

Possible role of coronal streamer as magnetically-closed structure in shock-induced energetic electrons and metric type II radio bursts

Xiangliang Kong¹, Yao Chen¹, Fan Guo², Shiwei Feng¹, Bing Wang¹, Guohui Du¹, and Gang Li³

ABSTRACT

Two solar type II radio bursts, separated by ~ 24 hours in time, are examined together. Both events are associated with coronal mass ejections (CMEs) erupting from the same active region (NOAA 11176) beneath a well-observed helmet streamer. We find that the type II emissions in both events ended once the CME/shock fronts passed the white-light streamer tip, which is presumably the magnetic cusp of the streamer. This leads us to conjecture that the closed magnetic arcades of the streamer may play a role in electron acceleration and type II excitation at coronal shocks. To examine such a conjecture, we conduct a test-particle simulation for electron dynamics within a large-scale partially-closed streamer magnetic configuration swept by a coronal shock. We find that the closed field lines play the role of an electron trap, via which the electrons are sent back to the shock front for multiple times, and therefore accelerated to high energies by the shock. Electrons with an initial energy of 300 eV can be accelerated to tens of keV concentrating at the loop apex close to the shock front with a counter-streaming distribution at most locations. These electrons are energetic enough to excite Langmuir waves and radio bursts. Considering the fact that most solar eruptions originate from closed field regions, we suggest that the scenario may be important to the generation of more metric type IIs. This study also provides an explanation to the general ending frequencies of metric type IIs at or above 20-30 MHz and the disconnection issue between metric and interplanetary type IIs.

¹Shandong Provincial Key Laboratory of Optical Astronomy and Solar-Terrestrial Environment, and Institute of Space Sciences, Shandong University, Weihai, Shandong 264209, China; yaochen@sdu.edu.cn

²Theoretical Division, Los Alamos National Laboratory, Los Alamos, NM 87545, USA

³Department of Space Science and CSPAR, University of Alabama in Huntsville, Huntsville, AL 35899, USA

Subject headings: acceleration of particles — shock waves — Sun: coronal mass ejections (CMEs) — Sun: radio radiation

1. Introduction

Streamers are the most prominent quasi-steady structures in the solar corona. Coronal Mass Ejections (CMEs) are observed to be closely related to and frequently interact with helmet streamers (e.g., Howard et al. 1985; Hundhausen 1993; McAllister & Hundhausen 1996; Chen et al. 2010, 2011; Feng et al. 2011; Chen 2013). In the streamer region, the Alfvénic speed is lower than that of the surroundings because of a much higher plasma density, and the plasma outflow is slow and hardly measurable in the closed magnetic field region (Habbal et al. 1997; Strachan et al. 2002; Kwon et al. 2013; Chen 2013). Due to these special plasma and magnetic conditions, the streamer structure is expected to facilitate the formation and/or enhancement of a CME-driven shock.

In recent studies, streamers are found to be important on the generation of type II radio bursts and the morphology of radio dynamic spectra. For example, it is suspected that the interaction region between CME/shock flanks and streamers is an important source of type II radio bursts (Reiner et al. 2003; Mancuso & Raymond 2004; Cho et al. 2007, 2008, 2011; Feng et al. 2012, 2013; Shen et al. 2013; Chen et al. 2014; Magdaleníć et al. 2014). Lately, Kong et al. (2012) and Feng et al. (2012, 2013) studied the effect of dense streamer structures on the type II spectra, and further inferred properties of the type II sources. According to the plasma emission mechanism, the type II radiation frequency is mainly determined by the local electron plasma density (Ginzburg & Zhelezniakov 1958; Nelson & Melrose 1985). Therefore, the type II spectral shape may change accordingly if dense structures (e.g., streamers) are present in the path of type II emitting sources. Two specific morphological features of type IIs relevant to CME-streamer interactions, namely, the spectral break and spectral bump, were identified. The spectral break appears as an abrupt change of the drifting rate of the type II spectrum while the bump appears as a plateau or bulge on the type II spectrum. Feng et al. (2013) also suggested that the type II source should be spatially compact with a spatial size less than 0.05-0.1 R_{\odot} , according to the overall bumping time of the emission lanes. Although the above studies are useful in unravelling the connection between type II bursts and CME-streamer interaction, how streamers are physically involved in electron acceleration and radio emission processes induced by a coronal shock remains unknown.

The observed type II bursts indicate the generation of nonthermal electrons close to

coronal shocks (Nelson & Melrose 1985). Previous studies often consider the acceleration of electrons at a planar shock (e.g., Holman & Pesses 1983; Wu 1984). However, it is known that this can only lead to strong acceleration when the shock normal is quasi-perpendicular to the incident magnetic field and the shock speed is high. Recent works have investigated nonplanar effects on the acceleration of particles. For instance, magnetic trapping geometries have been considered to be efficient particle accelerator when there exists large-scale magnetic turbulence interacting with a shock (e.g., Guo & Giacalone 2010; Guo et al. 2010), at the termination shock induced by a solar flare reconnection downflow (e.g., Somov & Kosugi 1997; Guo & Giacalone 2012; Nishizuka & Shibata 2013), and in the magnetotail dipolarization process during magnetic storms or substorms in the absence of a shock (e.g., Birn et al. 1997, 1998). As a CME-driven shock sweeps through a streamer, the shock front can intersect with the same magnetic field line at two different points. This leads to a similar magnetic trapping geometry likely important to shock-induced electron acceleration and type II excitation.

In this study, we explore the possible role of streamers as magnetically-closed structures in electron acceleration and excitation of metric type II radio bursts induced by a coronal shock from the following two aspects. We first present observations of two type II burst events to indicate that the closed structure of coronal streamer may be important to type II excitations. We then conduct a test-particle simulation to demonstrate that the shock-streamer system can lead to strong electron acceleration, validating the physical implication derived from observations. Conclusions and discussion are presented in the last section.

2. Observation of two metric type II radio bursts

In this section, we analyze the observational data of two metric type II radio bursts that occurred on 2011 March 25 and 27, with a ~ 24 -hour separation. The later event has been studied in detail by Kong et al. (2012). Here we first focus on the former event by examining the simultaneous radio spectra and CME imaging data. We then briefly summarize common observational features of the two events.

Figure 1 shows the radio dynamic spectrum between 23:13 UT and 23:39 UT on 2011 March 25. The data are a combination of Bruny Island Radio Spectrometer (BIRS; Erickson 1997) in the range of 10-35 MHz and Learmonth in the range of 35-180 MHz. The temporal resolution of both stations is 3 seconds. Other radio stations, such as Culgoora (Prestage et al. 1994) and Green Bank Solar Radio Burst Spectrometer (GBSRBS; White et al. 2006), also recorded this radio burst. Before the onset of the type II burst, we observe a fast-drifting type III radio burst at $\sim 23:15$ UT during the impulsive phase of an M1.0 GOES

soft X-ray flare. The type II burst starts at $\sim 23:17$ UT. Both the fundamental and harmonic bands can be identified, as denoted by “F” and “H” in Figure 1. From the harmonic band, we can obtain the average drift rate of the type II burst being ~ -0.18 MHz s^{-1} (~ -0.09 MHz s^{-1} for the fundamental band), and the ending time is $\sim 23:36$ UT. We can see some bump- or break- like morphological features of the slowly-drifting backbone. They are probably caused by the shock penetrating into or propagating across coronal density structures (Feng et al. 2012, 2013; Kong et al. 2012).

Now we examine imaging observations of the eruption process. The CMEs in these two events erupted from the same active region (AR) NOAA 11176. By combining the imaging data observed by the Solar Dynamics Observatory (SDO)/AIA (Lemen et al. 2012) and the Solar TERrestrial RELations Observatory (STEREO; Kaiser et al. 2008) and the magnetic field configuration obtained from the potential-field source-surface model (PFSS; Schatten et al. 1969; Schrijver & Derosa 2003), Kong et al. (2012) concluded that the AR was located at one foot of a large-scale streamer structure. On 2011 March 25, the location of the AR was S16E30, and STEREO A (B) was $\sim 89^\circ$ ahead ($\sim 95^\circ$ behind) of the Earth. Therefore, in the field of view (FOV) of the Earth the eruption is a solar disk event, while in the FOV of STEREO A a backside event near the east limb and in the FOV of STEREO B a front side event near the west limb. This greatly reduces the projection effect on measuring the CME front heights with STEREO.

Figure 2 shows the white light coronagraph data observed by STEREO/COR1 B between 23:20 UT and 23:55 UT. Panel (a) is the direct image at 23:20 UT and panels (b)-(h) are the running difference images. From these images we can see that an outward-propagating bright CME front moves through the streamer structure. The CME front becomes much weaker and more diffuse when passing over the main structure of the streamer. The blue triangles are the outlining streamer envelop depicted from panel (a) and over-plotted onto other panels, to indicate the relative location of the streamer and the CME front.

Heliocentric heights of the CME front measured along the streamer axis are shown as squares in the height-time plot in Figure 3, with blue for COR1 A and red for COR1 B. The measurement uncertainty of the heights from COR1 is estimated to be less than $0.05 R_\odot$ (~ 5 pixels). From the linear fit to the data points, we find that the mean speeds of the CME front at 23:25-23:40 UT are 514 ± 13 km s^{-1} (COR1 A) and 520 ± 29 km s^{-1} (COR1 B). At the time of the eruption, the temporal cadence of EUVI B in the 195 Å wavelength is 2.5 min, while it is 5 min for EUVI A. As noted above, the AR is on the backside as seen from STEREO A, therefore we only show the heights of the eruption front measured from EUVI B, as red triangles. The measurement uncertainty is estimated to be about $0.02 R_\odot$ (~ 10 pixels). Using the data points of both EUVI B and COR1 B, we can obtain the mean

speed of the CME front during the type II burst (23:17-23:36 UT) to be $\sim 620 \pm 25 \text{ km s}^{-1}$. In addition, in Figure 3 we also plot the heights of coronal EUV wave observed by AIA in 193 Å (taken from Kumar & Manoharan (2013)) with green plus signs.

With the mean speed of CME front ($\sim 620 \text{ km s}^{-1}$) and the two-fold Newkirk density model (Newkirk 1961), the type II spectrum can be fitted well as shown by the red solid line in Figure 1. To illustrate the influence of using different density models, we also present the fitting curves using one-fold (red dashed line) and three-fold (red dotted line) Newkirk model. It can be seen that these three lines can basically enclose the entire type II emissions. The heights of radio emission source deduced from the spectral fitting are shown in Figure 3 as three black straight lines. The dashed (solid, dotted) line represents the fitting curve with the 1-fold (2-fold, 3-fold) Newkirk density model. Comparing the heights of the coronal eruption front measured from the imaging observations by SDO and STEREO to the radio source heights obtained by the spectral fitting, we find that different data sets of heights are consistent with each other. On the other hand, from panels (c)-(h), there exists an apparent deflection of coronal ray/streamer on the southern flank of the CME corresponding to its lateral expansion, which indicates a fast-wave nature of the CME front. Based on these observations, we suggest that the type II burst was generated by the eruption-driven front (presumably the shock) from inside of the streamer. Such a suggestion is supported by many previous studies which provide important insights into the physical relation between the type-II-emitting shock and the EUV/white-light front (e.g., Biesecker et al. 2002; Vrsnak et al. 2006; Chen et al. 2014).

For the purpose of our study, it is important to determine the height of streamer cusp. The height can be estimated from the direct white-light image of the streamer as shown in Figure 2(a). The top of the outlining envelope can be used to determine the cusp location. To provide a consistency check, we examine carefully the difference images shown in Figure 2. From panels (e)-(g), we observe a rising bright cusp feature within the streamer envelope. The cusp stops rising after 23:50 UT till it becomes overlapping with the streamer envelope, and remains bright till 00:20 UT the next day. In the meanwhile, the CME front continues its outward propagation. The bright cusp-like difference structure is formed by the upwelling plasmas along the disturbed yet still-closed (or just-closed) streamer structure in the recovering phase of the post-eruption corona. These plasmas are contained by the closed field lines and accumulated there, as indicated by the observation that the cusp structure stops rising yet still remains bright after it coincides with the white-light streamer envelope. We therefore suggest that the cusp feature observed in panels (g) and (h) can be used to depict the closed streamer structure and to determine its cusp height. In addition, the same feature also appears in the base difference image (Figure 2(i)), providing a consistency check of our analysis. With this analysis, the cusp height is estimated to be at 2.2 - 2.4 R_{\odot} . Similar cusp

structure also appears both in the running difference and base difference images for the 2011 March 27 event (e.g., see Figure 4(f) in Kong et al. (2012)). The heights of streamer tip (cusp) are similar in both events.

It can be seen that the CME/shock front propagated across the streamer cusp region at 23:35-23:40 UT. In Figure 1 we see that the type II burst ends at $\sim 23:36$ UT. Therefore, within the observational uncertainty, we can infer that the type II ending time coincides with the time when the shock passed the streamer cusp.

For the event on 2011 March 27, the type II dynamic spectrum and the eruption process have been investigated in Kong et al. (2012). The main feature of that event is that the type II spectrum shows an intriguing break, i.e. the normal slowly-drifting emission being followed by a few fast-drifting bands. They suggested that the pre-break emission was produced by the shock propagating within the streamer, while the spectral break was caused by the radio-emitting shock crossing the streamer boundary along which the plasma density drops abruptly.

Some common observational features of the two events are summarized as follows: (1) Both CMEs erupted from the same AR beneath a well-observed helmet streamer, and the sweeping process of the CME front through the streamer structure can be observed clearly; (2) the heights of CME front obtained from imaging observations are consistent with that deduced from the type II spectral fitting using a reasonable density model; (3) type II radio emission ended when CME/shock fronts passed the streamer cusp region, subject to observational uncertainty. These observational results indicate that both type IIs were possibly related to the shock-streamer interaction. Especially, the last point leads us to conjecture that the type IIs are likely affected by the magnetically-closed streamer configuration. To test such an observational indication, we conduct test-particle simulation of electron acceleration in a streamer-shock system.

3. Test-particle simulation of electron acceleration in a streamer-shock system

In this section, we carry out a test-particle simulation to study the energization of electrons in a prescribed magnetic configuration consisting of a streamer and an outward-propagating shock. In Section 3.1, we introduce the initial configuration and parameter setup of the streamer-shock system and the test-particle simulation. In Section 3.2, we first analyze the trajectory and energy evolution of a typical electron to understand the acceleration mechanism; then we compare the distributions of electrons that are accelerated to different energies to identify the factors that affect the electron acceleration process; we

also present the energy spectra of energetic electrons.

3.1. Numerical Model

We use an analytical model for streamers given by Low (1986). It describes an axisymmetric magnetic structure containing both magnetic arcades and open field lines with a current sheet in a spherical coordinate (r, θ) . This model has been used in previous corona and solar wind modellings (e.g., Chen & Hu 2001; Hu et al. 2003a,b). In this study, the magnetic field strength in the polar region on the solar disk is set to be 10 G. The magnetic topology of the streamer in the region of interest is shown in Figure 4 under Cartesian coordinate (x, z) . The z -axis represents the rotation axis of the Sun, the x -axis is in the solar equatorial plane parallel to the streamer axis, and the y -axis completes the right-handed triad with the solar center being at the origin. The black lines represent magnetic field lines and the red line denotes the outermost closed field line and the current sheet above. The height of streamer cusp is taken to be $2.5 R_{\odot}$. The simulation domain is given by $x = [1.5, 3.0] R_{\odot}$ and $z = [-0.8, 0.8] R_{\odot}$, which includes some open fields surrounding the streamer. The y component of the magnetic field B_y is set to be 0. In the simulation domain, the average magnitude of magnetic field (B_0) is ~ 0.2 G.

For simplicity, we consider a planar shock propagating along the streamer axis, as shown by the dashed blue line in Figure 4. The shock is assumed to form at $x_0 = 1.5 R_{\odot}$ in the beginning of the simulation, consistent with previous studies of the formation heights of metric type II shocks (e.g., Pohjolainen 2008; Magdalenic et al. 2008; Nindos et al. 2011; Gopalswamy et al. 2009). The shock speed U_{sh} is taken to be 600 km s^{-1} . We also assume the shock is wider than the streamer. The calculation is carried out in the shock frame (x', y, z) , where the shock is at $x' = 0$, and the plasmas carrying the magnetic field flow from $x' < 0$ (upstream) with a speed of $U_1 \sim U_{sh}$ to $x' > 0$ (downstream) with a speed of U_2 . The flow speed close to the shock is given by a hyperbolic tangent function $U(x') = (U_1 + U_2)/2 - (U_1 - U_2) \tanh(x'/th)/2$, where U_1 and U_2 are the upstream and downstream flow speeds in the shock frame. The shock compression ratio is assumed to be $U_1/U_2 = 4$ for simplicity. th is the shock thickness and is taken to be $0.01 U_1/\Omega_{ci}$, where Ω_{ci} is the proton gyrofrequency defined by B_0 . Using a larger value of $th \sim 0.1 U_1/\Omega_{ci}$ in the simulation (not shown here) does not change our results considerably.

After the shock starts to propagate outward from $1.5 R_{\odot}$, electrons with an initial energy $E_0 = 300 \text{ eV}$ are continuously injected at a constant rate at $x' = -10 U_1/\Omega_{ci}$ in the upstream. The initial pitch angles of the electrons are given randomly. For each electron, the equation of motion under the Lorentz force is solved in the shock frame. The electron

mass is taken to be $1/1836$ of the proton mass. The numerical technique used to integrate electron trajectories is the Bulirsch-Stoer method (Press 1986), which has been widely used in calculating particle trajectories (e.g., Guo & Giacalone 2014). The algorithm uses an adjustable time-step method based on the evaluation of the local truncation error. It is highly accurate and has been tested to conserve particle energy to a very good degree. In this study, a total of 1.5×10^6 electrons are injected. When an electron moves out of the simulation domain or reaches a distance of $10^4 U_1/\Omega_{ci}$ downstream of the shock, we stop tracking it and terminate the calculation. An *ad hoc* pitch-angle scattering is included to mimic the effects of coronal plasma turbulence, kinetic waves on electron and ion scales, and Coulomb collisions (e.g., Marsch 2006). This is done by randomly changing the electron pitch angle every $\tau = 10^4 \Omega_{ci}^{-1}$.

3.2. Simulation Results

The simulation results show that low energy electrons can be accelerated to an energy up to several hundred times the initial energy E_0 . We first analyze the simulation result for an electron that is accelerated to $\sim 25 E_0$ to show the shock acceleration mechanism.

In Figure 5, we display the electron trajectory in the x - z lab frame (panel a) and in the x' - z shock frame (panel c). The blue arrows in these two panels point to the injection point of the electron. From panel (c) we can see that the electron propagates in the closed field and interacts with the shock front multiple times. Panels (b) and (d) show its position x and x' over time, respectively. The dashed blue line in panel (b) indicates the position of the outward propagating shock, while that in panel (d) indicates the shock front ($x' = 0$) in the shock frame. The vertical red dotted lines denote the electron reflection points at the shock. As seen from our simulation results, at the shock an electron can either get reflected back to the upstream or go through the shock moving to the downstream. This is mainly determined by the exact value of the electron pitch angle and the magnetic field variation induced by the shock. As the shock passes over a closed field line, the electrons moving along that field line are left behind in the downstream.

In panels (e)-(f) we present the temporal evolution of the electron drifting distance along the y direction and the temporal evolution of its energy in the shock frame. It can be seen that a fast drift in the y direction is accompanied by a simultaneous sharp increase of the electron energy whenever the electron is reflected at the shock (see the vertical red dotted lines). Therefore, the electron gains energy mainly during its gradient- \mathbf{B} drift along the shock-induced electric field ($-\mathbf{U} \times \mathbf{B}$). In other words, the electron is accelerated via the well-known shock drift acceleration (SDA) mechanism (also called the fast Fermi acceleration

at a quasi-perpendicular shock) (Armstrong et al. 1985; Wu 1984).

It can be seen from Figures 5(c) and 4(d) that an electron may also change its direction besides reflection at the shock front ($x' = 0$). This is due to the pitch angle scattering of electrons. To examine the effect of such scattering on our result, we also conduct simulations without any scattering. In the above case (with a random scattering every $\tau = 10^4 \Omega_{ci}^{-1}$), electrons can be energized up to $\sim 530 E_0$, and the fractions of electrons accelerated to $>5 E_0$, $>10 E_0$, $>20 E_0$ and $>30 E_0$ are $\sim 8.4\%$, 3.9% , 1.1% and 0.39% , respectively. In comparison, for the case without any scattering, the highest electron energy obtained is $\sim 48 E_0$, and the fractions of electrons accelerated to $>5 E_0$, $>10 E_0$, $>20 E_0$ and $>30 E_0$ reduce to $\sim 2.4\%$, 0.25% , 0.005% and 0.002% , respectively. This suggests that the scattering effect plays an important role in the electron acceleration process, which allows electrons to get more chance to encounter the shock front and thus receive more accelerations. Recent spacecraft observations and numerical simulations have shown that whistler waves and small-scale shock ripples can play a role in scattering electrons in pitch-angle at the shock front (Burgess 2006; Guo & Giacalone 2010; Wilson et al. 2012). Indeed, enhanced scattering implies a diffusive shock acceleration (DSA) process. Note that although the effect of pitch angle scattering can affect our quantitative results, it does not change the main conclusion of this study.

To analyze other physical factors affecting the acceleration, we examine the distribution of injection position of electrons that have achieved a final energy of $5\text{-}10 E_0$, $10\text{-}20 E_0$, $20\text{-}30 E_0$ and $>30 E_0$. Figure 6 presents this distribution. The most obvious feature of this figure is that none of the electrons that are injected in the open field regions are accelerated to $>5 E_0$. In other words, only electrons injected in the closed field region can be efficiently accelerated by the SDA mechanism of the study. Note, however, we do not include the effect of perpendicular diffusion due to, e.g., large-scale magnetic turbulence (e.g., Giacalone & Jokipii 1999). The same conclusion is obtained in the case without any scattering. This highlights the importance of the large-scale closed magnetic field in shock-induced electron acceleration.

In addition, fewer accelerated electrons have an injection position further away from the streamer axis ($|z| > 0.4\text{-}0.5 R_\odot$). This may be partly due to the location-dependent shock geometry. To illustrate this point, in Figure 7 we show variations of θ_{Bn} (the angle between the upstream magnetic field line and the shock normal) with z at different distances ($x = 1.5, 1.6, 1.8$ and $2.0 R_\odot$). We find that the shock is more quasi-perpendicular ($\theta_{Bn} > 45^\circ$) closer to the streamer axis, and more quasi-parallel ($\theta_{Bn} < 45^\circ$) further away from the streamer axis. According to earlier studies, the quasi-perpendicular shock geometry favors electron acceleration (e.g., Holman & Pesses 1983; Wu 1984; Guo & Giacalone 2010). This is consistent with our simulation result. Another factor which may contribute to this is that

generally electrons moving along shorter loops (with injection locations closer to the streamer axis) need less time to approach the shock front, thus less time is required for further electron reflection and acceleration. Nevertheless, only few electrons that are injected very close to the streamer axis ($|z| < 0.02-0.03 R_\odot$) are accelerated, as seen from this figure. Possible explanations for this result are twofold. First, these electrons are released right atop of closed field lines and the shock front is nearly parallel to the upstream field and about to embrace the field line, so there may not be enough time for electrons to get repetitive accelerations. Second, as pointed out by Holman & Pesses (1983), if θ_{Bn} is very close to 90° , the reflection condition can not be satisfied, therefore these electrons can not receive efficient acceleration.

Now we examine the electron positions at 9 different times when the shock propagates to distances of 1.6, 1.7, 1.8, ..., $2.4 R_\odot$. These data sets are superposed onto the streamer field lines and shown together in Figure 8, where the scattering points represent electrons that have been accelerated to 5-10 E_0 (panel a), 10-20 E_0 (b), 20-30 E_0 (c), and $>30 E_0$ (d). It can be seen that energetic electrons mainly concentrate in the shock upstream within its immediate neighborhood, and close to the streamer axis (i.e., around the tip of the relevant closed field lines). In the above paragraph, we have presented the two possible factors making the electron acceleration at the loop apex (close to the streamer axis) more efficient.

In addition, electrons of higher energies are more concentrated in a narrower region. Electrons shown in panels (c) and (d) have energy of $>20-30 E_0$ ($>6-9$ keV with an electron velocity of $>0.15-0.2 c$, c is the speed of light). Previous studies suggest that electron beams with such high energies are capable of exciting Langmuir waves and radio emission (e.g., Ergun et al. 1998; Mann & Klassen 2005). Thus, it is reasonable to regard that the region with $>20-30 E_0$ electrons is the likely source of the radio bursts. As seen from panels (c) and (d), the region with energetic electrons (presumed to be the radio source region) concentrate around the top of the closed field lines with a radial extension of only a few hundredths R_\odot and a latitudinal extension of a few tenths R_\odot . In other words, according our simulation, the outermost part of a closed field line is filled with electrons that are energetic enough to excite Langmuir oscillations and may become radio loud while the field line is about to be embraced by the shock. This simulation result provides an explanation to the well-known fact that the type II emission is generally confined to fairly narrow frequency bands as shown in Figure 1.

Figure 9 shows the energy spectra at the 9 instants (corresponding to different shock heights) as presented in Figure 8. The vertical coordinate is given by the number of energetic electrons (ΔN) in a certain energy range ($\Delta(E/E_0)$). We can see all these energy spectra can be well approximated by a power-law spectra with an index of ~ -3 . It is well known

that the DSA mechanism of energetic particle acceleration is capable of producing power-law spectra while the SDA mechanism in the scattering-free limit not (Bell 1978; Wu 1984). The reason we get a power-law spectrum via the SDA mechanism here is due to the fact that electrons repetitively travel back to the shock and get accelerated because of the trapping effect of closed field lines and the weak pitch-angle scattering, physically equivalent to the diffusive process in DSA theory. Note similar power-law spectra have been found in previous simulations within the framework of SDA mechanism (e.g., Burgess 2006; Guo & Giacalone 2010).

In addition, energetic electrons as modeled here are bi-directional. Figure 10 shows the pitch angle distribution of energetic electrons ($E > 5 E_0$) in the shock upstream. We can see that at most times it indicates a counter-streaming distribution. Counter-streaming electrons may give rise to counter-propagating Langmuir waves and strong harmonic emission (Ganse et al. 2012, 2014). This, as well as the power-law distribution, may be important to the excitation of enhanced Langmuir waves and type II bursts and should be considered in type II theories and simulations (e.g., Schmidt & Cairns 2012a,b, 2014).

In the above text, we have demonstrated that the closed field lines play the role of an electron trap, via which the electrons are sent back to the shock front multiple times, and therefore accelerated to high energies by the shock. We note that the present model is rather simplified and the case of a planar shock wider than the streamer and therefore the shock intersecting at two points with the same field line is a best case scenario. In the case of the shock having only one intersection with the streamer closed field, then the trapping will be realized by the shock and the magnetic mirror at the other end of the tube, the acceleration time may become much longer. It should be further extended by a parameter study on the effect of the streamer configuration, the shock geometry, compression ratio, as well as the scattering effect by coronal waves and turbulence. In addition, a more realistic streamer configuration with a self-consistent eruption-generated magnetohydrodynamic shock, like those simulated by Rousev et al. (2004) and Chen et al. (2007), should be adopted.

4. Conclusions and Discussion

In this paper we first examine two coronal type II events occurring on 2011 March 25 and 2011 March 27 and present their common observational features (as follows). (1) Both events erupted from the same AR below a streamer structure, and the sweeping process of the CME front across the streamer structure can be well observed; (2) In both events, the heights of the CME fronts as measured with the coronagraph data are consistent with that deduced from the type II spectral fittings; (3) Both type II bursts ended once the CME

fronts passed the streamer cusp, subject to observational uncertainty. These observations, especially the last point, lead us to conjecture that the closed field topology of the streamer may be important to the shock acceleration of the type-II-emitting energetic electrons.

To validate this conjecture, we perform a test-particle simulation of electron acceleration in a shock-streamer system. Simulation results show that only those electrons that are injected within the closed field regions can be accelerated efficiently. The trapping effect of the closed streamer structure allows the electrons to return to the shock front multiple times and be repetitively accelerated via the SDA mechanism. It is shown that energetic electrons mainly concentrate around the tips of relevant closed field lines in the shock upstream, and are almost counter-streaming with energy spectra approximated by a power-law with an index of ~ -3 . This predicts some features of the energetic electrons and the possible source location of the type II radio bursts, and provides an explanation to the well-known narrowband feature of type II bursts. The simulation forms a basis for further studies with a more realistic configuration.

Our study highlights the possible role of large-scale magnetically closed structures, as a trapping agency of energetic electrons, in shock-induced electron acceleration and metric type II excitation. It is well known that a majority of solar eruptions originate from closed field regions above the AR. If the eruption-induced shock (either the flare blast wave or the CME-driven shock) is formed inside the streamer, a streamer-shock configuration as described here can arise. Obviously the generation of such a configuration is not limited to streamers. For any coronal loops or magnetic arcades, if the shock is excited within them, an equivalent particle acceleration system can present. Therefore, electron acceleration by a shock propagating in a closed field structure may be important to the generation of metric type IIs in more events. Note that the scenario should be considered as complementary to any shock acceleration mechanism. We do not intend to reject any other theories or processes of shock-electron acceleration, e.g., those considering the effect of shock ripples (Guo & Giacalone 2010), turbulence (Guo & Giacalone 2010), and whistler waves (Oka et al. 2006; Wilson et al. 2012).

The relationship between coronal/metric type IIs and interplanetary (IP) type IIs is a long-standing problem with debate. As observed in radio dynamic spectra, metric and IP type IIs often do not join with each other, and many metric type IIs do not have IP counterparts (e.g., Gopalswamy et al. 2001; Cane & Erickson 2005). At present, two scenarios are proposed for such observations. The first scenario proposes that the Alfvénic speed maximum, which is reached at $\sim 3-4 R_{\odot}$, is responsible for the type II discontinuity since the shock gets weakened or even disappeared at this Alfvén maximum (Mann et al. 1999, 2003; Gopalswamy et al. 2001; Vršnak et al. 2002). The other scenario suggests that

the metric and IP type IIs are produced by shocks of different origins. The IP type IIs are generated by the interplanetary CME-driven shock, while the coronal type IIs may be from the flare-driven blast wave (e.g., Gopalswamy et al. 1998; Cane & Erickson 2005). However, the latter suggestion regarding the metric type II origin still suffers from hot debate (see the recent review by Vršnak & Cliver (2008)).

In this study, we provide an alternative explanation. We suggest that there are metric type IIs that are closely related to the closed field structures (e.g., streamers and coronal loops). Once the shock goes beyond the outermost part of the closed field structures, the metric type IIs may stop accordingly. Observationally, it is known that many coronal type IIs end at frequencies above $\sim 20\text{-}30$ MHz (e.g., Nelson & Melrose 1985; Shanmugaraju et al. 2003). These termination frequencies correspond to the heliocentric coronal heights of $2\text{-}3 R_{\odot}$ according to broadly-used density models (e.g., Newkirk 1961; Saito 1970). On the other hand, it is generally believed that coronal magnetic field structures are closed below this distance. For IP type IIs and the rare type II events that can extend from metric to decameter/hectometric wavelength (e.g., Cane & Erickson 2005), their generations are certainly not completely determined by the large-scale closed coronal structures, and should be explained differently (e.g., Bale et al. 1999; Pulupa & Bale 2008).

The simulation of Schmidt & Cairns (2014) and relevant studies of the same group of authors represent the state-of-the-art study in type II theory and simulation. Their simulation is able to explain some important observational features of type IIs, including the type II frequencies, emission intensities, the overall drift rate and the spectral intermittencies. They also make some predictions about the radio emitting locations. For example, the sources may be away from the shock nose and may change with time as θ_{Bn} changes), and the emission intensities are greatly affected by the interaction of CMEs with coronal and interplanetary structures. In comparison, we notice that their simulation predicts a weak emission at the shock-streamer interaction region due to the change of θ_{Bn} there. This seems to be inconsistent with some observations that the CME-streamer interaction region is important to type II bursts (see our introduction). In the Schmidt & Cairns study, the type II emissivity is mainly determined by the shock speed (strength) and the shock geometry (the value of θ_{Bn}). The trapping effect of closed field lines on shock electron acceleration, as well as the effect of counter-streaming electrons on type II emissivity have not been considered. This might be the reason of the above inconsistency.

We are grateful to the STEREO, SDO, BIRS, and Learmonth teams for making their data available to us. This work was supported by grants NSBRSF 2012CB825601, NNSFC 41274175 and 41331068. Gang Li’s work at UAHuntsville was supported by NSF grants ATM-0847719 and AGS1135432.

REFERENCES

- Armstrong, T. P., Pesses, M. E., & Decker, R. B. 1985, in AGU Geophys. Monograph Ser. 35, Collisionless Shocks in the Heliosphere: Reviews of Current Research, ed. B. T. Tsurutani & R. G. Stone (Washington, DC: American Geophysical Union), 27
- Bale, S. D., Reiner, M. J., Bougeret, J.-L., et al. 1999, *Geophys. Res. Lett.*, 26, 1573
- Bell, A. R. 1978, *MNRAS*, 182, 147
- Biesecker, D. A., Myers, D. C., Thompson, B. J., Hammer, D. M., & Vourlidas, A. 2002, *ApJ*, 569, 1009
- Birn, J., Thomsen, M. F., Borovsky, J. E., et al. 1997, *JGR*, 102, 2325
- Birn, J., Thomsen, M. F., Borovsky, J. E., et al. 1998, *JGR*, 103, 9235
- Burgess, D. 2006, *ApJ*, 653, 316
- Cane, H. V., & Erickson, W. C. 2005, *ApJ*, 623, 1180
- Chen, Y. 2013, *Chin Sci Bull*, 58, 1599
- Chen, Y., Du, G. H., Feng, L., et al. 2014, *ApJ*, 787, 59
- Chen, Y., Feng, S. W., Li, B., et al. 2011, *ApJ*, 728, 147
- Chen, Y., & Hu, Y. Q. 2001, *SoPh*, 199, 371
- Chen, Y., Hu, Y. Q., & Sun, S. J. 2007, *ApJ*, 665, 1421
- Chen, Y., Song, H. Q., Li, B., et al. 2010, *ApJ*, 714, 644
- Cho, K. S., Bong, S. C., Kim, Y. H., et al. 2008, *A&A*, 491, 873
- Cho, K. S., Bong, S. C., Moon, Y. J., et al. 2011, *A&A*, 530, 16
- Cho, K. S., Lee, J., Gary, D. E., Moon, Y. J., & Park, Y. D. 2007, *ApJ*, 665, 799
- Ergun, R. E., Larson, D., Lin, R.P., et al. 1998, *ApJ*, 503, 435
- Erickson, W. C. 1997, *PASA*, 14, 3, 278
- Feng, S. W., Chen, Y., Kong, X. L., et al. 2012, *ApJ*, 753, 21
- Feng, S. W., Chen, Y., Kong, X. L., et al. 2013, *ApJ*, 767, 29

- Feng, S. W., Chen, Y., Li, B., et al. 2011, *SoPh*, 272, 119
- Ganse, U., Kilian, P., Vainio, R., Spanier, F. 2012, *SoPh*, 280, 551
- Ganse, U., Kilian, P., Spanier, F., Vainio, R. 2014, *A&A*, 564, A15
- Giacalone, J., & Jokipii, J. R. 1999, *ApJ*, 520, 204
- Ginzburg, V. L., & Zhelezniakov, V. V. 1958, *SvA*, 2, 653
- Gopalswamy, N., Kaiser, M. L., Lepping, R. P., et al. 1998, *JGR*, 103, 307
- Gopalswamy, N., Lara, A., Kaiser, M. L., & Bougeret, J.-L. 2001, *JGR*, 106, 25261
- Gopalswamy, N., Thompson, W. T., Davila, J. M., et al. 2009, *SoPh*, 259, 227
- Guo, F., & Giacalone, J. 2010, *ApJ*, 715, 406
- Guo, F., Jokipii, J. R., & Kota, J. 2010, *ApJ*, 725, 128
- Guo, F., & Giacalone, J. 2012, *ApJ*, 753, 28
- Guo, F., & Giacalone, J. 2014, *ApJ*, 780, 16
- Habbal, S. R., Woo, R., Fineschi, S. et al. 1997, *ApJ*, 489, L103
- Holman, G. D., & Pesses, M. E. 1983, *ApJ*, 267, 837
- Howard, R. A., Sheeley, N. R., Jr., Michels, D. J., Koomen, M. J. 1985, *JGR*, 90, 8173
- Hu, Y. Q., Li, G. Q., & Xing, X. Y. 2003a, *JGR*, 108(A2), 1072
- Hu, Y. Q., Habbal, S. R., Chen, Y., & Li, X. 2003b, *JGR*, 108(A10), 1377
- Hundhausen, A. J. 1993, *JGR*, 98(A8), 13177
- Kaiser, M. L., Kucera, T. A., Davila, J. M., et al. 2008, *SSRv*, 136, 5
- Kong, X. L., Chen, Y., Li, G., et al. 2012, *ApJ*, 750, 158
- Kumar, P., & Manoharan, P. K. 2013, *A&A*, 553, A109
- Kwon, R.Y., Kramar, M., Wang, T. J. et a. 2013, *ApJ*, 776, 55
- Lemen, J. R., Title, A. M., Akin, D. J., et al. 2012, *Sol. Phys.*, 275, 17
- Low, B. C. 1986, *ApJ*, 310, 953

- McAllister, A. H., & Hundhausen, A. J. 1996, in: Balasubramanian, K.S., Keil, S.L., Smartt, R.N. (eds.) *Solar Drivers of the Interplanetary and Terrestrial Disturbances*, ASP Conf. Ser. 95, 171
- Magdalenić, J., Vršnak, B., Pohjolainen, S., et al. 2008, *Sol. Phys.*, 253, 305
- Magdalenić, J., Marqué, C., Krupar, V., et al. 2014, *ApJ*, 791, 115
- Mancuso, S., & Raymond, J. C. 2004, *A&A*, 413, 363
- Mann, G., & Klassen, A. 2005, *A&A*, 441, 319
- Mann, G., Klassen, A., Aurass, H., & Classen, H.-T. 2003, *A&A*, 400, 329
- Mann, G., Klassen, A., Estel, C., & Thompson, B. J. 1999, *ESASP*, 446, 477
- Marsch, E. 2006, *Living Reviews in Solar Physics*, 3, 1
- Nelson, G. J., & Melrose, D. B. 1985, in *Solar Radiophysics*, ed. D. J. McLean & N. R. Labrum (Cambridge: Cambridge Univ. Press), 333
- Newkirk, G., Jr. 1961, *ApJ*, 133, 983
- Nindos, A., Alissandrakis, C. E., Hillaris, A., & Perka-Papadema, P. 2011, *A&A*, 531, 31
- Nishizuka, N. & Shibata, K. 2013, *PRL*, 110, 051101
- Pohjolainen, S. 2008, *A&A*, 483, 297
- Oka, M., Terasawa, T., Seki, Y., et al. 2006, *GRL*, 33, L24104
- Press, W. H., Flannery, B. P., Teukolsky, S. A., & Vetterling, W. T. 1986, *Numerical Recipes* (Cambridge: Cambridge Univ. Press)
- Prestage, N. P., Luckhurst, R. G., Paterson, B. R., Bevins, C. S., & Yuile, C.G. 1994, *Sol. Phys.*, 150, 393
- Pulupa, M., & Bale, S. D. 2008, *ApJ*, 676, 1330
- Roussev, I. I., Sokolov, I. V., Forbes, T. G., et al. 2004, *ApJ*, 605, L73
- Reiner, M. J., Vourlidas, A., Cyr, O. C. St., et al. 2003, *ApJ*, 590, 533
- Saito, K. 1970, *Ann. Tokyo Astron. Obs.*, 12, 53
- Schatten, K. H., Wilcox, J. M., & Ness, N. F. 1969, *Sol. Phys.*, 6, 442

- Schmidt, J. M., & Cairns, Iver H., 2012a, JGR, 117, A04106
- Schmidt, J. M., & Cairns, Iver H., 2012b, JGR, 117, A11104
- Schmidt, J. M., & Cairns, Iver H., 2014, JGR, 119, 69
- Schrijver, C. J., & Derosa, M. L., 2003, Sol. Phys., 212, 165
- Shanmugaraju, A., Moon, Y. J., Dryer, M., Umapathy, S. 2003, SoPh, 215, 161
- Shen, C. L., Liao, C. J., Wang, Y. M., Ye, P. Z., & Wang, S. 2013, SoPh, 282, 543
- Somov, B. V., & Kosugi, T. 1997, ApJ, 485, 859
- Strachan, L., Suleiman, R., Panasyuk, A. V., Biesecker, D. A., & Kohl, J. L. 2002, ApJ, 571, 1008
- Vršnak, B., Aurass, H., Magdalenić, J., & Mann, G. 2002, A&A, 396, 673
- Vršnak, B., & Cliver, E. W. 2008, SoPh, 253, 215
- Vršnak, B., Warmuth, A., Temmer, M., et al. 2006, A&A, 448, 739
- White, S. M., Bastian, T. S., Bradley, R., Parashare, C., & Wye, L. 2006, in ASP Conf. Ser. 345, From Clark Lake to the LongWavelength Array: Bill Ericksons Radio Science, ed. N Kassim et al. (San Francisco: ASP), 176
- Wilson, L. B., III, Koval, A., Szabo, A., et al. 2012, GRL, 39, L08109
- Wu, C. S. 1984, J. Geophys. Res., 89, 8857

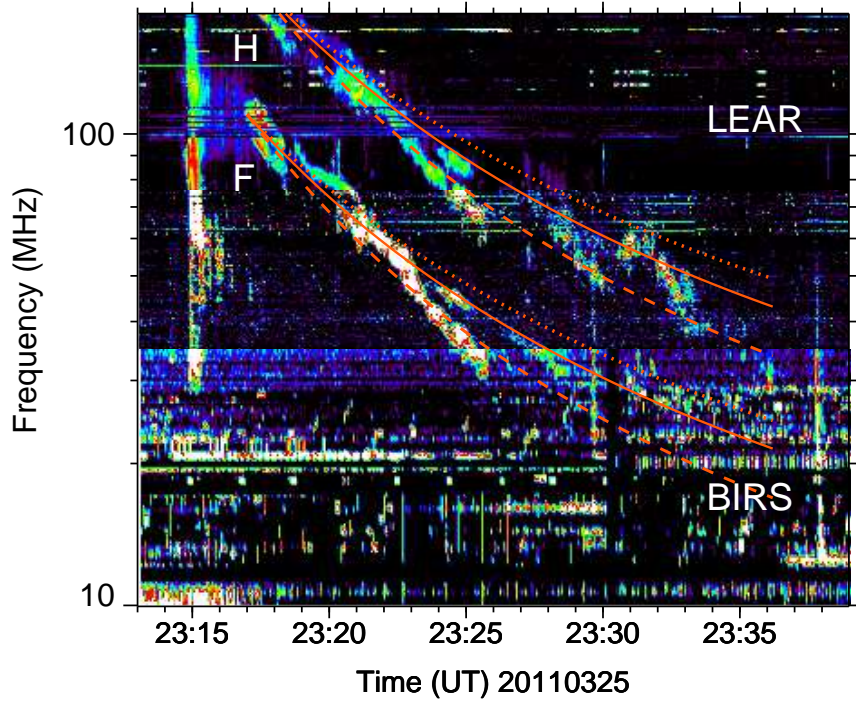


Fig. 1.— The radio dynamic spectrum on 2011 March 25 as recorded by BIRS (10-35 MHz) and Learmonth (35-180 MHz) radio spectrometers. “F” and “H” denote the fundamental and harmonic bands of the type II burst. The red lines are the fitting curves using 1-fold (dashed), 2-fold (solid) and 3-fold (dotted) Newkirk density model and a shock speed of 620 km s^{-1} , respectively.

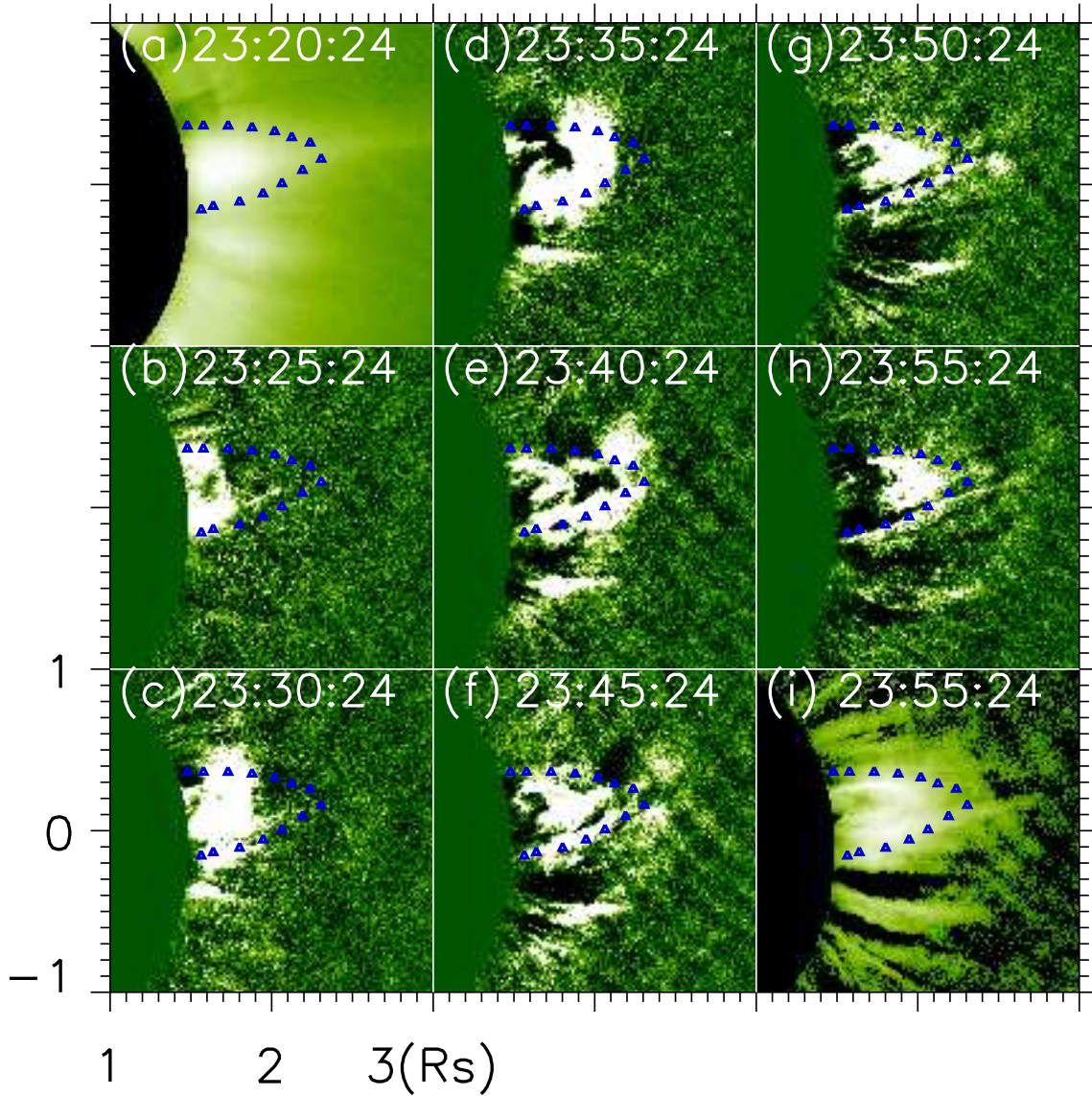


Fig. 2.— STEREO/COR1 B white light data at 23:20-23:55 UT on 2011 March 25. Panel (a) is the direct image, panels (b)-(h) are running difference images, and panel (i) is the base difference image (23:55 UT - 23:20 UT). The blue triangles are the outlining streamer envelop depicted from panel (a) and over-plotted onto other panels to indicate the relative location of the streamer and the CME front.

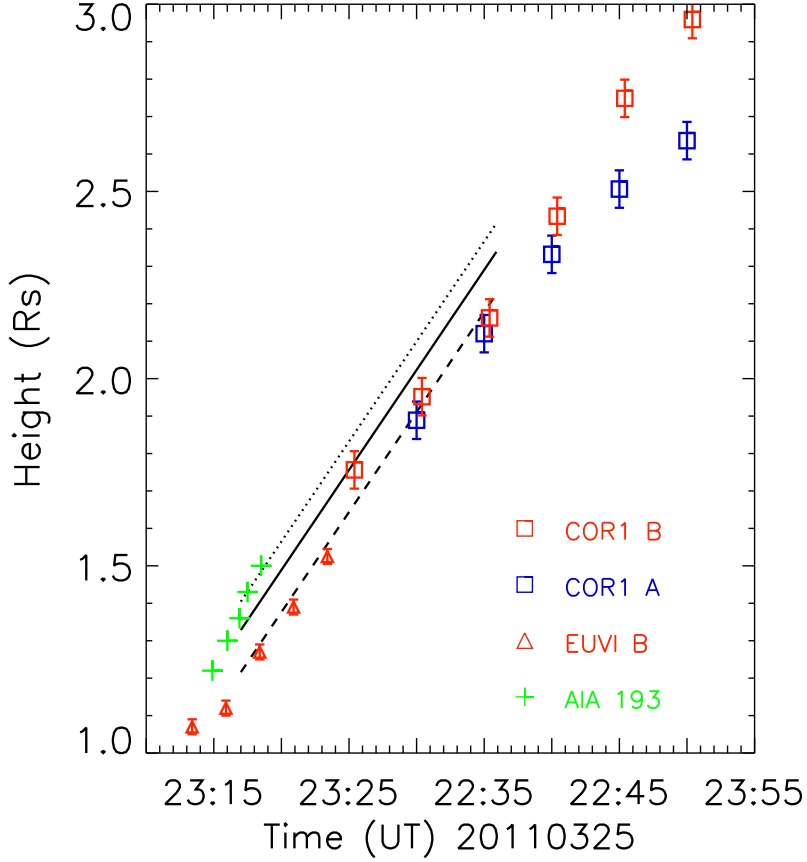


Fig. 3.— The heliocentric heights of CME fronts measured from COR1 A (blue squares), COR1 B (red squares) and EUVI B (red triangles). The error bars indicate measurement uncertainties of the heights, estimated to be $\sim 0.05 R_{\odot}$ for COR1 and $\sim 0.02 R_{\odot}$ for EUVI. The green “+” signs are heights of coronal EUV wave observed by AIA in 193 \AA (taken from Kumar & Manoharan (2013)). The heights of the radio source deduced from the type II spectral fittings (see Figure 1) are shown as three black straight lines.

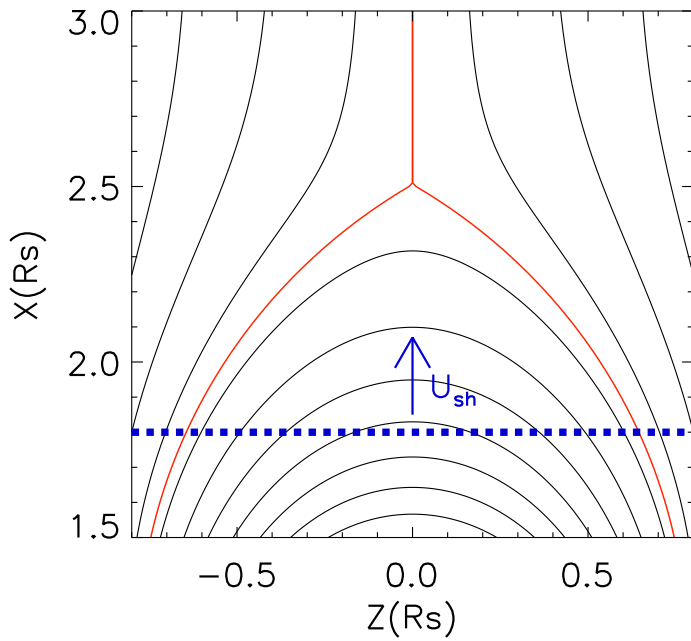


Fig. 4.— The streamer-shock configuration in the numerical simulation. The streamer magnetic field is given by an analytical model in Low (1986). The black lines represent magnetic field lines, the line in red presents the outermost closed field line and the current sheet above, and the height of streamer cusp is taken to be $2.5 R_{\odot}$. A planar shock front propagating along the streamer axis is shown by the blue dashed line.

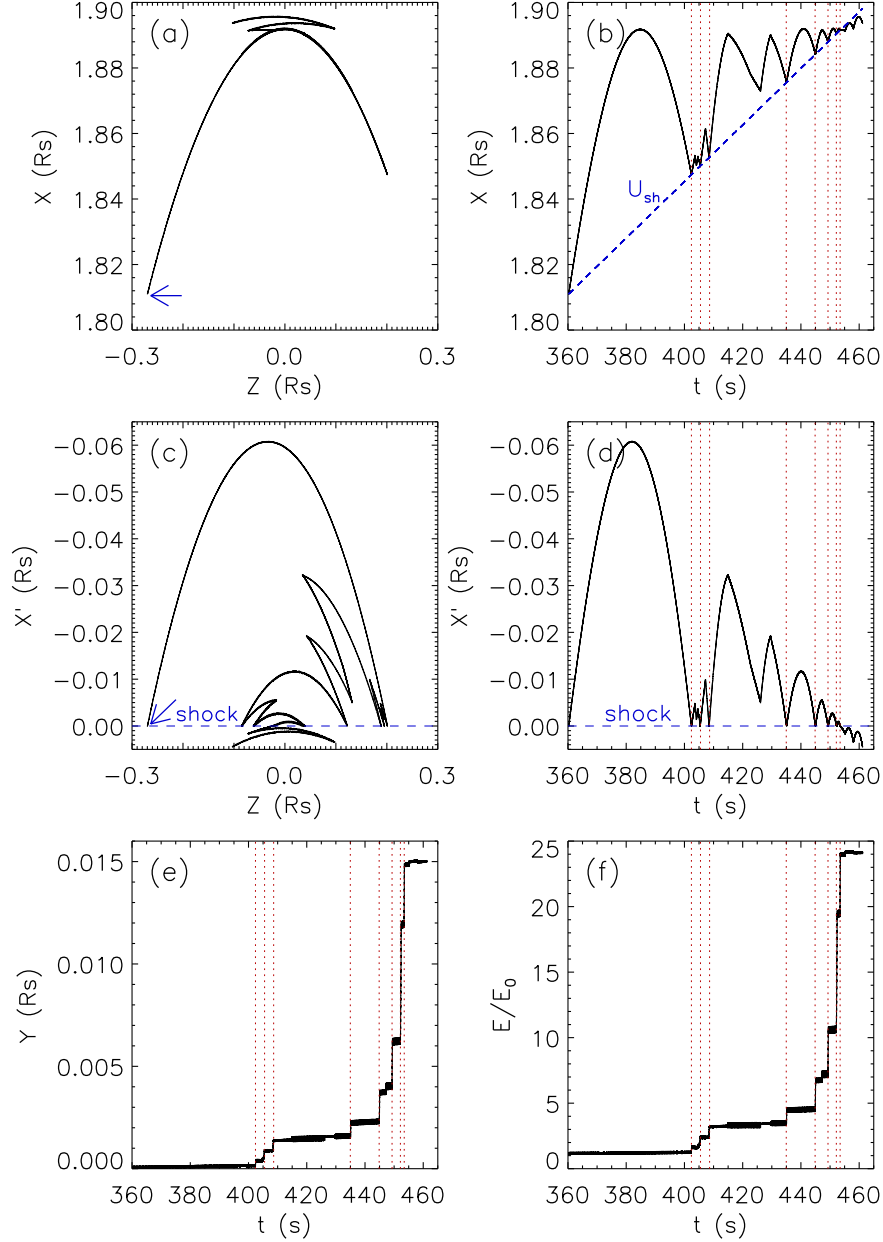


Fig. 5.— Simulation results for an electron that is accelerated to $\sim 25 E_0$. Panels (a) and (c) display the electron trajectory in the x - z lab frame and in the x' - z shock frame. The blue arrows in the two panels point to the injection point of the electron. Panels (b) and (d) show its position x and x' over time, respectively. The dashed blue line in panel (b) indicates the position of the outward propagating shock, while that in panels (c) and (d) represents the shock front ($x' = 0$) in the shock frame. Panels (e)-(f) present the temporal evolution of the electron drifting distance along the y direction and the temporal evolution of its energy in the shock frame. The vertical red dotted lines denote the electron reflection points at the shock.

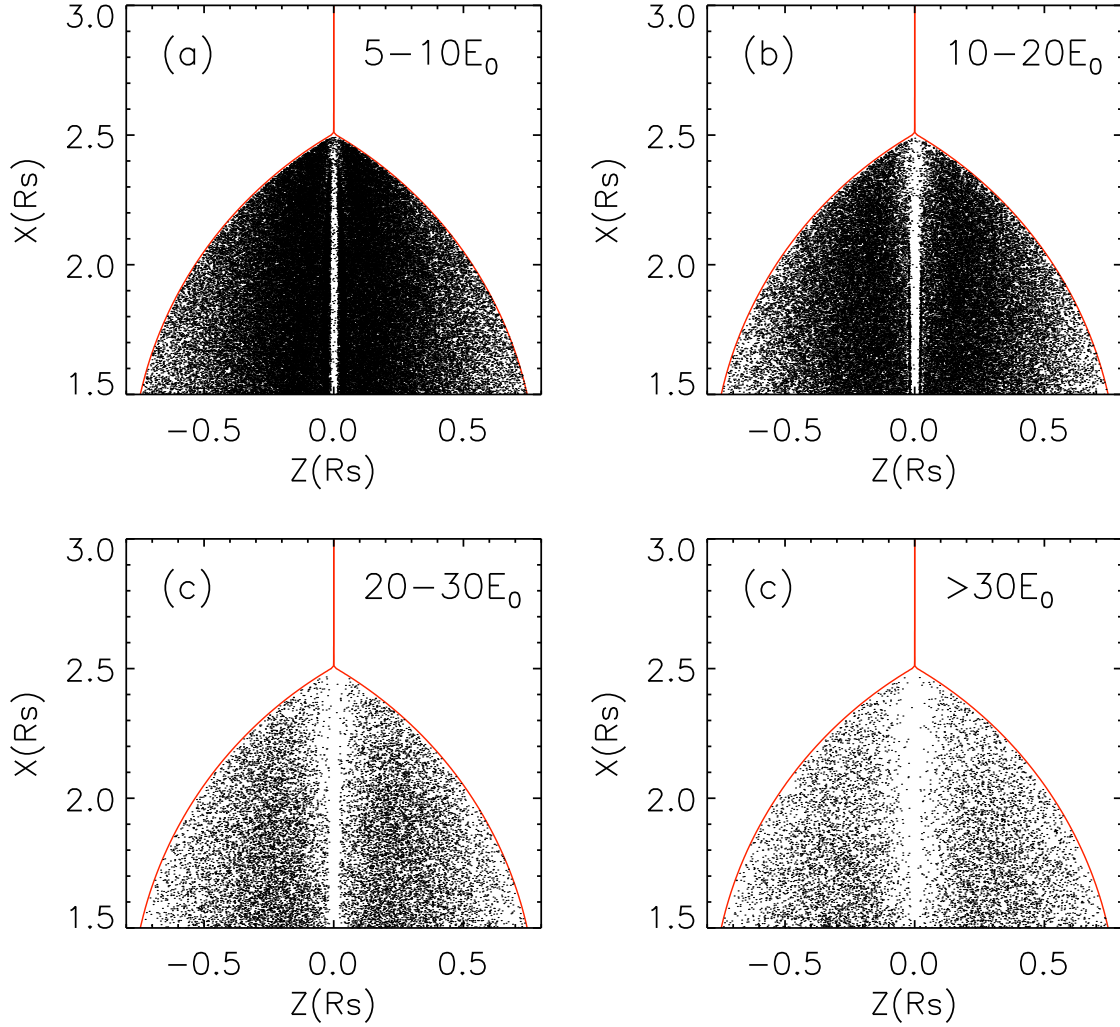


Fig. 6.— The distribution of injection position of electrons that have achieved a final energy of $5-10 E_0$, $10-20 E_0$, $20-30 E_0$ and $>30 E_0$, respectively.

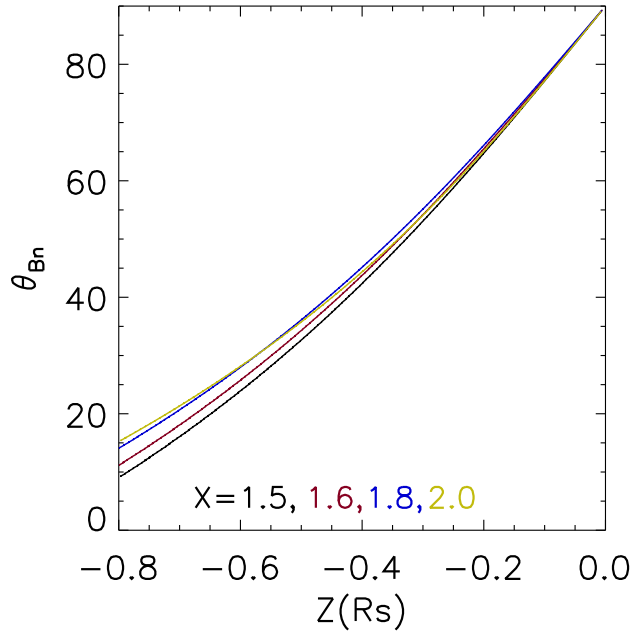


Fig. 7.— Variations of θ_{Bn} (the angle between the upstream magnetic field line and the shock normal) with z at different distances ($x = 1.5, 1.6, 1.8$ and $2.0 R_\odot$).

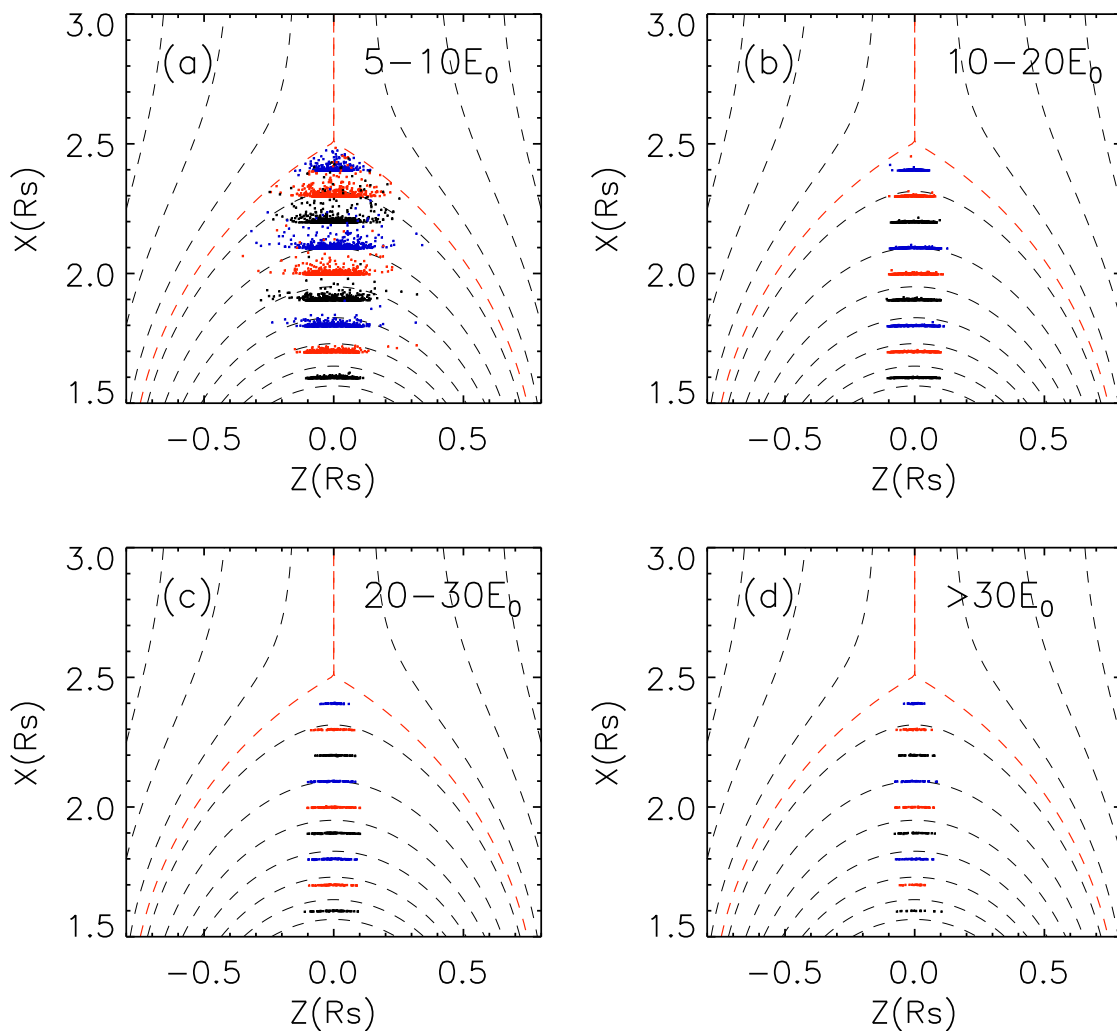


Fig. 8.— The electron positions at several different times when the shock propagates to distances of 1.6, 1.7, 1.8, ..., $2.4 R_\odot$. These 9 different data sets are superposed onto the streamer field lines, where the scattering points in panels (a)-(d) represent electrons that have been accelerated to $5-10 E_0$, $10-20 E_0$, $20-30 E_0$, and $>30 E_0$, respectively.

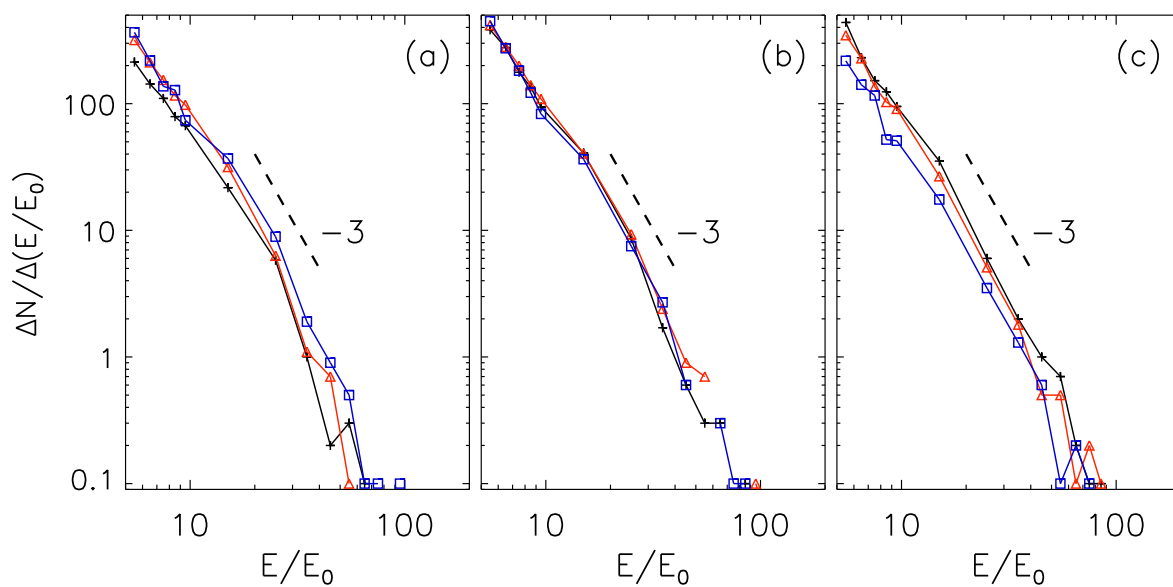


Fig. 9.— The electron energy spectra at the 9 different times (corresponding to different shock heights $x = 1.6, 1.7, 1.8, \dots, 2.4 R_{\odot}$) as presented in Figure 8, shown in each panel as black pluses, red triangles and blue squares with increasing shock heights. In panel (a): $x = 1.6, 1.7, 1.8 R_{\odot}$; panel (b): $x = 1.9, 2.0, 2.1 R_{\odot}$; panel (c): $x = 2.2, 2.3, 2.4 R_{\odot}$. The black dashed line represents a -3 power-law spectrum.

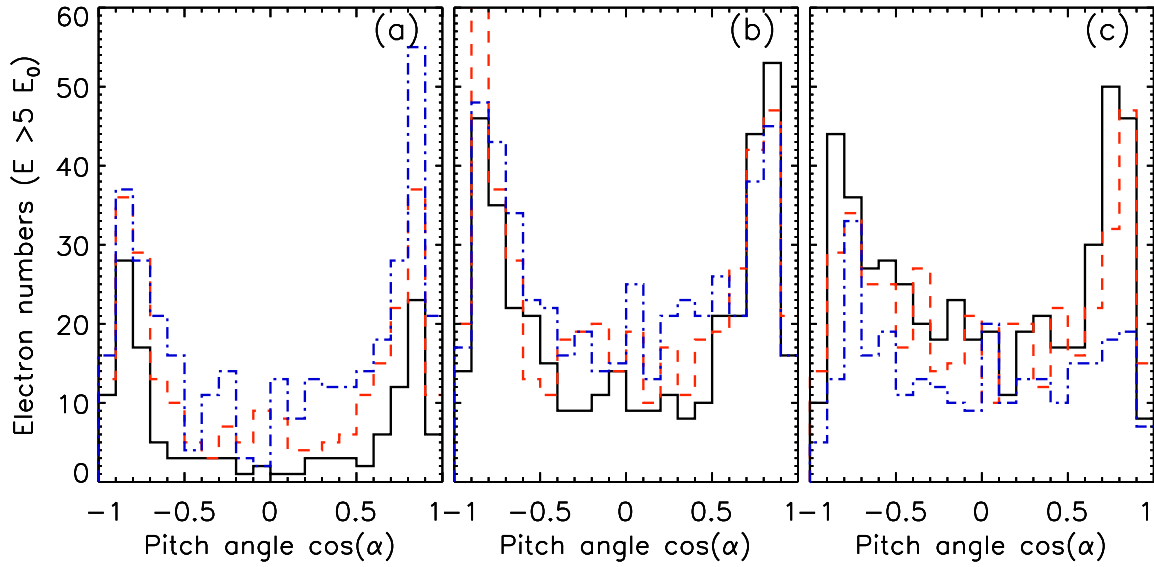


Fig. 10.— The electron pitch angle at the 9 different times (corresponding to different shock heights $x = 1.6, 1.7, 1.8, \dots, 2.4 R_{\odot}$) as presented in Figure 8, shown in each panel as black solid lines, red dash line and blue dash-dot line with increasing shock heights. In panel (a): $x = 1.6, 1.7, 1.8 R_{\odot}$; panel (b): $x = 1.9, 2.0, 2.1 R_{\odot}$; panel (c): $x = 2.2, 2.3, 2.4 R_{\odot}$.